

Towards experimental process parameter development for Ti-6Al-4V TPMS lattice structures with application to small scale dental implants using micrographs

A. Jahn^{1*}, H. Li¹, N. Emminghaus¹, T. Melnyk¹, J. Hermsdorf¹, and S. Kaierle^{1,2}

¹Laser Zentrum Hannover e.V., Hollerithallee 8, 30419 Hannover, Germany

²Leibniz Universität Hannover, Institut für Transport- und Automatisierungstechnik, An der Universität 2,
30823 Garbsen, Germany

*Corresponding author: a.jahn@lzh.de

Abstract

Ti-6Al-4V is a widely used alloy in implant engineering and lattice structures can be applied to locally match the stiffness of the implant to the stiffness of bone. Triply periodic minimal surface (TPMS) structures are popular due to their curved surface, which supports a good manufacturability and osseointegration of the implant. Tests with different TPMS structures showed a strong interaction between design factors and manufacturing parameters resulting in the need for individual parameter development. However, to the best of our knowledge, the most work in the current literature focusses on mechanical and biological examinations of TPMS structures manufactured with standard parameters. As process parameters influence the structural properties, the optimum values for further analysis may not have been investigated (e.g., their influence on microstructure and mechanical properties). In this work, a design of experiments approach is used to develop process parameters. As computer tomography scans are resource intensive for large scale parameter development, a sparser approach using micrographs for porosity analysis is introduced. Small structures with unit cell size as small as 1.0 mm are fabricated on a laser powder bed fusion industrial machine. Our initial studies show that the design factor pore size is negligible in comparison to wall thickness when optimizing internal porosity.

Keywords: Additive Manufacturing, Ti-6Al-4V, Laser powder bed fusion, Gyroids, Porosity

Introduction

With its advantage to manufacture customized products with a high design freedom, a main focus area of Additive Manufacturing (AM) and especially Laser Powder Bed Fusion (LPBF) are biomedical applications. Here, porous metallic structures for bone scaffolds and orthopedic implants were researched in the past years [1]. Ti-6Al-4V alloy is widely utilized in implant applications due to its biocompatibility. However, the stiffness of bulk Ti-6Al-4V is significantly higher than that of human bone, which ranges between 10.0 GPa and 30.0 GPa. This difference in stiffness can result in stress shielding, potentially leading to failure of the implant or the surrounding bone [2]. To adjust the mechanical and biological properties of implants to that of the human bone, porous structures (e.g., lattices) can be used. Lattice structures are three-dimensional open-celled structures that are organized in a topological manner, consisting of one or more repeating unit cells [3]. Through tailoring pore architecture, pore volume and percentage of porosity the unit cell properties, like the elastic modulus can be adjusted [4].

A popular design of lattice structures is one with triply periodic minimal surfaces (TPMS). These structures include minimal surfaces and display periodicity in three dimensions based on the theory of differential geometry with a mean curvature of zero [5]. This feature of TPMS structures is similar to the one of bone [6, 7]. Different factors such as relative density and periodicity can be adjusted to enhance their mechanical properties [8]. TPMS scaffolds have certain inherent advantages over strut-based ones. For strut-based lattices, the LPBF process constraints the inclination angle, as the upper layers need support from the previous ones. For TPMS such a constraint does not exist as with the continuous curvature the layers are supported which improves the

manufacturability of the lattice [8]. Research also indicates that the curvature of implant surfaces is critical for stimulating bone growth [9]. Due to their similarity in shape to natural trabecular bone and the three-dimensional curvature of their surfaces, TPMS lattice structures potentially offer better bone fixation compared to strut-based lattice structures [10]. Bobbert et al. also studied the properties of TPMS structures. They likewise showed that the porous metallic biomaterials based on TPMS have similar topological, mechanical, and physical properties close to trabecular bone. It was also presented that TPMS structures have relatively low elastic properties, high yield strengths and fatigue resistance that is similar or better than bone. These properties decrease the stress shielding phenomena of implants and categorize TPMS structures as suitable mechanical support for bone tissue regeneration and osseointegration. Additionally, the permeability was similar to the data for trabecular bone [11].

The mechanical and biological properties of TPMS structures have been under intensive research focus in the last years. In this context, parts with TPMS structures for further analysis were mostly manufactured with the parameters provided by the equipment manufacturer based on the powder feedstock, e.g. in Ma et al. [12]. In LPBF based manufacturing, it is possible for irregularities to occur in the produced structures. These irregularities can manifest as defects or internal pores, residual powders, high or non-homogeneous surface roughness, and variations in thickness within the struts or walls. It is important to note that these irregularities can have a significant impact on the mechanical properties of additively manufactured parts and scaffolds, such as stiffness, compressive strength, and fatigue life [13].

The manufacturing outcomes are influenced by various process parameters, including laser parameters (such as speed, power, and beam size), powder properties (such as mean particle size), and layer thickness [14]. By optimizing these process parameters, it is possible to reduce the presence of defects [15, 16]. Therefore, when manufacturing lattice structures using LPBF, it is crucial to carefully select and optimize the process parameters to ensure optimal performance.

Various authors have researched this aspect [17]. Vilardell et al. proposed that special optimization of process parameters is necessary for thin-walled parts, as they observed that manufactured lattice structures showed deviations in wall thickness in comparison with the generated design and the lower relative density had an impact on the mechanical properties of porous structures [18]. Mahmoud et al. investigated various process parameters for graded gyroid structures and found that different parameters affected the relative density and strut size, consequently influencing the failure mode [19]. Hedayati et al. discovered that irregularities within the cross-section of struts in LPBF-processed Ti-6Al-4V scaffolds led to a decrease in stiffness and fatigue life [20]. Ma et al. examined the mechanical properties of gyroid scaffolds produced through LPBF. They compared the results obtained from simulations with experimental data and identified a discrepancy primarily attributed to manufacturing defects. As a result, the authors concluded that it is crucial to investigate processing parameters specifically tailored for porous parts in order to minimize the disparity between experimental and simulated outcomes [12]. Du Plessis et al. established a correlation between the performance of gyroids and microporosity, highlighting the significance of high density (absence of micro porosity in struts) for strength (static compression) and fatigue life [21]. Kelly et al. conducted a study on the fatigue characteristics of sheet-based gyroid scaffolds produced through LPBF using Ti-6Al-4V powder. They observed that void porosity within the gyroid walls served as initiation points for cracks, in contrast to the rough surface typically associated with LPBF. However, by adjusting the process parameters, they observed a change in the occurrence and distribution of voids. This reduction in defects led to enhanced fatigue life in both compression and tension tests [22]. The research also identified overall energy input as the primary factor influencing the occurrence of defects. This energy input can be determined by considering laser power, scan speed, and laser spot diameter. It was observed that higher energy input increased the likelihood of internal porosity within the struts [23, 24].

Bobbert et al. examined the properties of different types of TPMS structures manufactured with LPBF and stated that the optimization of process parameters for each designed porosity of the different types of minimal surfaces is necessary. Also, Kelly et al. concluded from their studies on the manufacturing and mechanical behavior of different gyroid structures that the new microarchitectures and designs should be studied in an iterative loop between design and process optimization [22]. Although process parameter development has been

performed extensively in research, it needs to be considered that the process parameter development highly depends on the machine and material used, as stated by Hanzl et al.[25].

The summarized work in the above paragraphs did not focus on small-scale structures (i.e., structures with unit cell of 1.0-2.0 mm). For analysis, e.g., of internal porosity or dimensional accuracy, mostly micro-computer tomography (μ CT) was used. Another method used to measure density is the Archimedes principle. While voids that are inherent in the manufactured part, cannot be detected with the Archimedes method, the disadvantage of μ CT is the resource intensity (expensive hard- and software, computational time, manual effort to adjust settings for the pore analysis). Thus, the analysis of micrographs could offer a compromise solution.

This work is part of an applied multi-disciplinary research group to develop dental implants with patient specific properties. This study contributes to the process parameter development for TPMS small-scale lattices (i.e., unit cells of as small as 1.0 mm dimension). Conducted pre-studies showed a strong interaction of design factors and process parameter, with the need for design specific process parameter optimization. With the same process parameter, some TPMS designs can be manufactured while others cannot be built, as depicted in Figure 11.

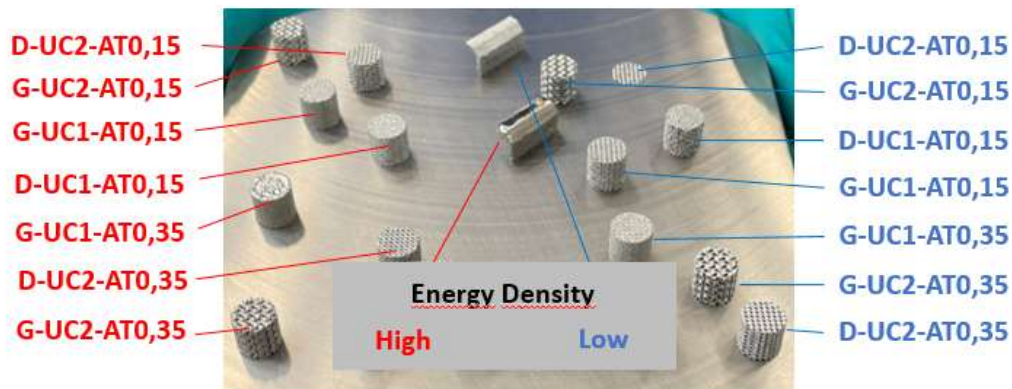


Figure 1: TPMS structure manufactured with different energy density (high/ low).
description: cell type (G gyroid/ /D diamand) – UC (Unitcell size 1/2mm)
– AT (thickness of wall 0.15/0.35 mm)

As cell type gyroid structures are chosen, since their mechanical and biological properties are even favorable in comparison to that of other TPMS unit cells [26, 27]. Gyroid structures are defined by the following parametric equation:

$$G = \cos\left(\frac{2\pi}{L} x\right) \sin\left(\frac{2\pi}{L} y\right) + \cos\left(\frac{2\pi}{L} y\right) \sin\left(\frac{2\pi}{L} z\right) + \cos\left(\frac{2\pi}{L} z\right) \sin\left(\frac{2\pi}{L} x\right) - t = 0 \quad (1)$$

where L is the size of each unit cell and t is the “level constant” that controls the volume fraction of each cell. From the further four design factors (wall thickness, pore size, unit cell size, porosity) at least two need to be defined to have a clear identification of the intended TPMS design.

To optimize the manufacturing process parameters, a design of experiment (DOE) approach is used. The design of TPMS lattice structures is defined by different factors as mentioned before (e.g. cell type, unit cell size, etc.). In addition, in LPBF more than 50 process parameters are known [28]. Considering the design and process parameters, a large experimental plan would be needed. Thus, the DOE process is often divided into the three steps (Screening, Modelling, Optimization) [29].

For the first step of Screening, Kleppmann suggests a procedure to reduce the number of factors by pre-considerations [30]. The process parameters that have the most significant impact on the formation of defects are those that determine the volumetric energy density (VED). The VED represents the amount of energy absorbed by a given volume of powder and can be calculated using key process parameters such as laser power (P), scan speed (v), hatch spacing (h), and layer thickness (t), as shown in Equation 1 [31], [32].

$$VED = \frac{P}{v \cdot t \cdot h} \quad (2)$$

Previous experiments on the same equipment and material had shown that optimized process parameter for dense parts include a layer thickness of 0.03 mm [33].

As the process of experimental parameter development is resource intensive, in this manuscript also a method to evaluate internal porosity from micrographs is introduced. The micrograph analysis method is verified in comparison to CT data. In the following the first results in application of this porosity measurement method are introduced. The porosity within the printed walls is called internal porosity or micro-porosity. It is differentiated from the overall porosity or macro-porosity (also given as 1 – volume fraction) of the lattice structure.

Materials and Methods

Material and equipment

In this work, powder Ti-6Al-4V Grade 23, supplied by ECKART TLS GmbH, is used for LPBF based additive manufacturing. The powder has a nearly spherical shape and the particle size ranges from 20.0 to 53.0 μm . Experiments are conducted on an industrial machine (Lasertec 12 SLM by DMG MORI) with a 400 W fiber laser (1070 nm, continuous wave, minimum spot diameter of 35 μm) is used.

Methods for analysis

After manufacturing of each specimen, these specimens are subjected to an extended cleaning procedure based on an ultrasonic cleaner using isopropanol.

Following X-ray tomography, scans were performed with a GE Nanotom S system. The full samples were scanned at 6.24 μm voxel size, using 90 kV and 110 μA , and 2400 images in a full rotation. The analysis from μCT data was performed by the software Volume Graphics VGSTUDIOMAX 3.5. First, the filtering is done using a non-local means filter with a smoothing factor of 1.2. Afterwards, the surface determination is performed with the advanced classical mode and a search distance of 20 voxels. Later, the Easy pore method of Volume Graphics was applied. The above approach thus led us to quantify the porosity.

For the microscopic examination, the specimens were embedded in epoxy resin followed by mechanical grinding and polishing for four layers of each specimens. Afterwards, for layers, pictures were taken with a Leica DM6 microscope with a focus of 2.5. An image specification of 5364 pixel by 4944 pixel is used.

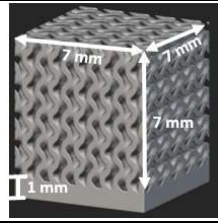
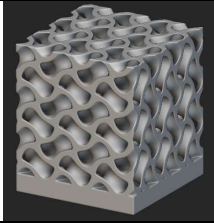
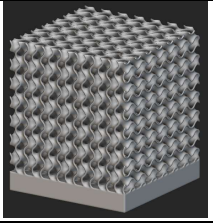
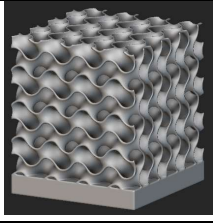
Design of experiments

The experiments include four factors, two design factors and two process factors are chosen to manufacture the sheet-gyroid structures. The first design factor is wall thickness. With the above mentioned spot size a minimal feature size lies at about 70 μm and a minimal wall thicknesses of 100 μm is chosen. Pore size is defined as the second examined design criteria in this DOE, as bone in-growth depends on the size of the cavity.

Thus, four different gyroid topologies were manufactured by altering wall thickness (100 and 300 μm) and designed pore size (400 and 800 μm), resulting in an overall porosity between 38 to 83 percent. The values were chosen in consideration of optimal pore sizes and volume fractions of TPMS structures related to human bone [10].

The specimens are cubes of $7 \times 7 \times 7 \text{ mm}^3$ size and were designed with the software nTopology and exported as STL. A solid base layer of 1 mm was added to the part for easier removal from the build plate and numbering. For better powder removal after manufacturing holes of 0.4 mm diameter were designed into it.

Table 1: Overview of chosen designs

Design factor	Specifications			
	Gyroid	Gyroid	Gyroid	Gyroid
Cell type	Gyroid	Gyroid	Gyroid	Gyroid
Wall thickness	300 μm	300 μm	100 μm	100 μm
Designed pore size/ cavity	400 μm	800 μm	400 μm	800 μm
Cell size	1400 μm	2200 μm	1000 μm	1800 μm
Overall porosity	38%	59%	70%	83%
				

The two selected process parameters are laser power and scan speed based on the considerations regarding VED above. The intention of this DOE step was the examination of the span of the process window. Thus, factor levels were chosen as intended extrema considering the mentioned screening trials and manufacturers suggestions for full structures (Table 2).

Table 2: Factor level combinations during modelling step of DOE

Process parameter combination	Laser power	Scan speed
1	70 W	800 mm/s
2	70 W	1000 mm/s
3	135 W	800 mm/s
4	135 W	1000 mm/s

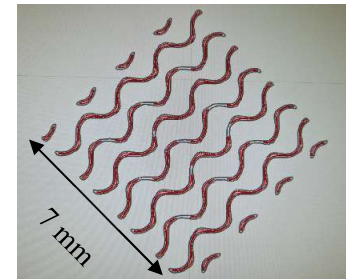


Figure 2: Layer of sliced and hatched gyroid

The layer thickness is kept constant at 0.03 mm (upper constraint based on previous experiments, lower constraint based on powder size). Hatch distance is kept constant 0.085 mm (standard machine parameter) since one can see from the sliced and hatched design in Figure 2 that most layers only include contour lines (red).

Thus, in this modelling phase a 2^4 factorial design with 16 experiments and 2 runs is chosen including the design factors, wall thickness and pore size, and process factors, laser power, and scan speed. To outline the experimental plan and perform the ANOVA the software JMP 15 is used.

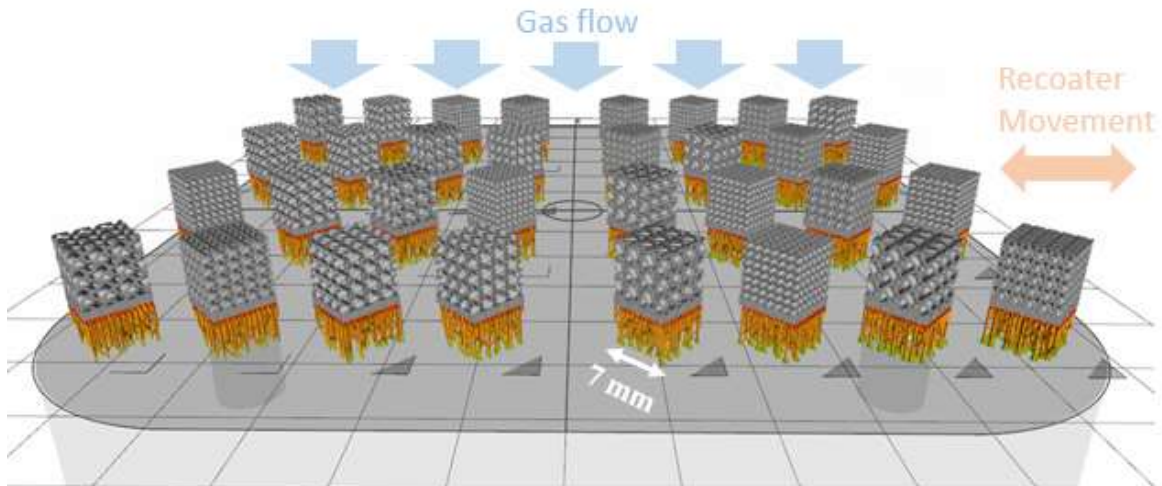


Figure 3: Build job layout

Code for micro-porosity analysis

To analyze the images for internal porosity and the manufactured overall porosity per volume fraction, a python-based script was developed. In this work, the manufacturing of complex shapes and surfaces such as the gyroid structures is addressed. Therefore, a robust and advanced algorithm was needed to enhance the traditional codes used on bulk material with a simple black-white comparison.

In the following, a short description of the developed code's flowchart (Figure 4) is given. For reference, the code is provided in the appendix. First, the algorithm uses different pre-processing methods. Contrast enhancement techniques are employed to improve the visibility and distinguishability of features within the images. Additionally, grayscale conversion prepares the image for binarization. In the subsequent step, the binarization process allows for the extraction of the foreground and removal of irrelevant information. Besides, morphological operations help to fill gaps and connect small, disjointed regions. After pre-processing, the contour detection is conducted. Pores in our images can be categorized into four groups (i.e., tiny pores: <100 pixel, small to medium pores: based on the given minimum and maximum value and pores with a small opening, designed cavities). The designed cavities are categorized to contribute to the overall porosity (1- volume fraction). The last ones are not included in the calculation of internal porosity, but in the calculation of the manufactured overall porosity. When searching for tiny pores, only the binary images were used without any additional preprocessing methods. This was done to avoid the possibility of losing these pores through other preprocessing techniques.

In addition, the morphological operation (opening and closing) with the big kernel is used for pores with a small connection to the surface as a preprocessing step. In case the algorithm finds overlapping pores due to an overlapping categorization, the outermost one is used. Then the algorithm iterates through each contour and calculates the internal area. The ratio of white pixels within the contour to the whole contour area is then calculated. If the ratio is below 30 percent, it indicates that the contour is likely a pore. The 30 percent threshold was found experimentally and through observations. Otherwise, the algorithm would include false irregularities based on specimen cutting and etching and due to the fact that also sintered-on powder can be found inside pores. Finally, the internal porosity is determined by dividing the sum of all pore areas by the total area of all pores and all white pixel. When calculating the overall porosity per manufactured volume fraction, first the rectangular region of interest (ROI) is determined around the specimen. Then a sub-image is extracted based on the coordinates of the bounding box. Finally, the manufactured volume fraction of the rectangular region is calculated by dividing the number of black pixels by the total number of pixels.

The code was applied on the 16 specimens of the first run. For each specimen an average of the internal porosity was calculated based on the four layer pictures.

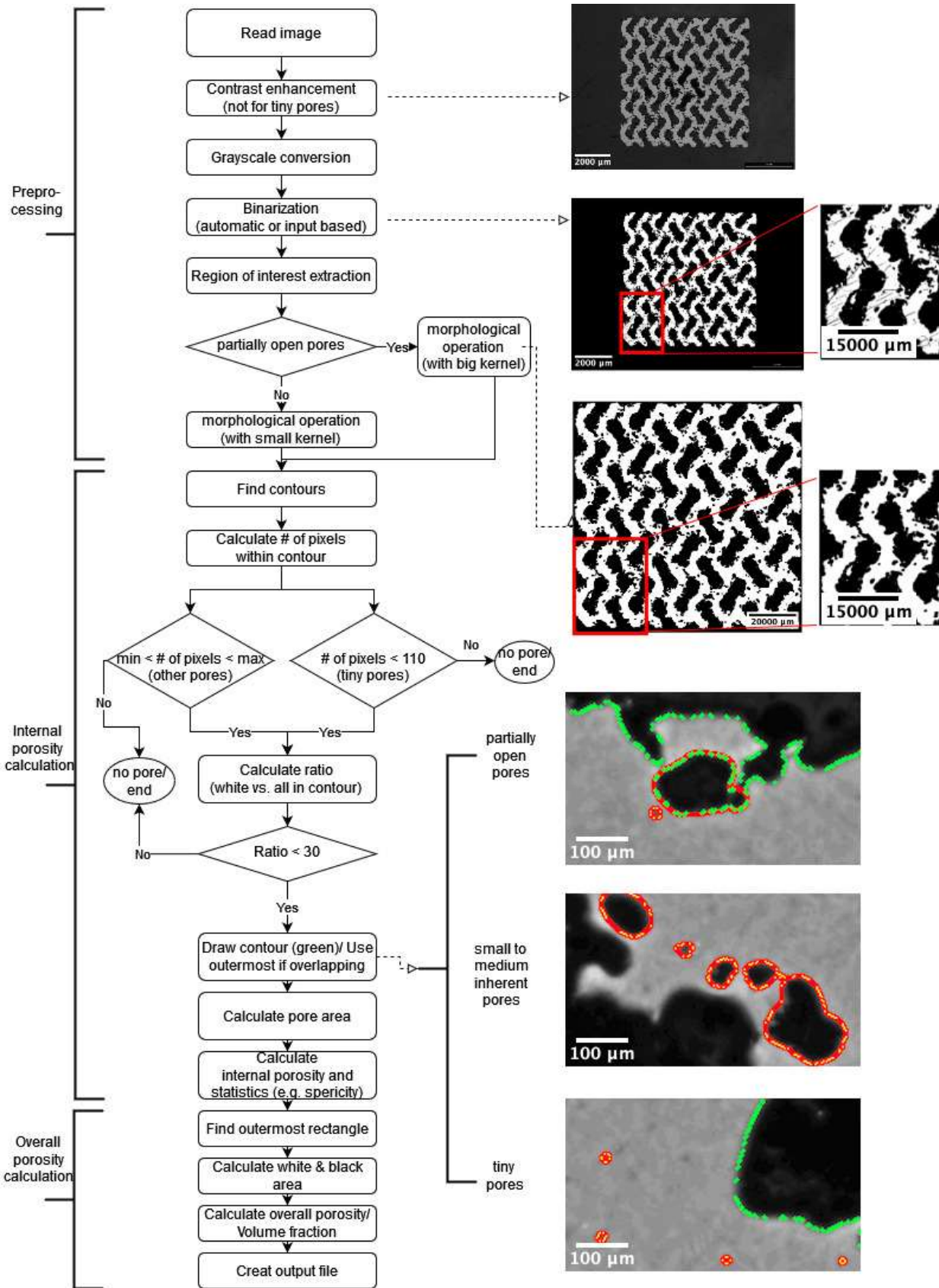


Figure 4: Flowchart of the developed code for porosity analysis

Results and Discussion

In the following, the results regarding internal porosity are examined after applying the developed code to the images. First, the results are validated in comparison with CT scans. Afterwards, first preliminary results of the DOE modelling step are presented.

Verification of the code

The complete experimental plan including the internal porosity results is included in Table 5. For some selected specimens the internal porosity was calculated from the CT data and compared to the micrographs. Parts 10, 11, 14 and 15 were chosen with the background to use different designs and manufacturing parameters. An overview of the results comparing the micrographs versus the CT images is given in Table 3.

In summary, it can be seen that the results of micrographs and CT images correlate well (parts 10, 14, 15). However, the values from the micrographs are higher than from the CT data. As a main reason for this difference, we see the fact that micrographs only include information on the current cross-section. That means, wherever the code found a black area surrounded by white pixels (the dense material) and fulfills the threshold requirements regarding size, a pore was found by the algorithm and included into the porosity calculation. It is not considered whether the cavity is connected to the surface in an adjacent layer and thus may not be a pore. On the other hand, the CT data involves information of the whole part. As the surface determination was executed on the CT data before the pore analysis, it can be differentiated for each layer what is real pore area (surrounded by dense material, visible in blue color in the CT pictures) and what are incisions of the surface (visible in the CT pictures as white bordered contours within other contours). For example, the CT excerpt of part 10 shows two bordered artefacts (A), which belong to the surface. However, in the etched images such artefacts are categorized as pores.

For part 11 the analysis of the micrographs shows a lower inherent porosity value than the CT data. This is evaluated as an outlier. From analyzing the CT data, artefacts can be seen on the edges. This is caused by the rotation during the CT scan. Therefore, the CT porosity analysis was repeated for a ROI in the center. From Table 4 it can be seen that the value of the inherent porosity reduced by about 40 percent excluding the shades and artifacts from the side. However, the calculated porosity in the CT data is still higher than that in the micrographs. The explanation for this can be found in the ROI CT images layer 1 and 2. These layers were randomly chosen in the CT data. It can be seen that most pores are located close to the surface indicating that the determination of such rough surface was difficult. The micrographs do not show such a phenomena. It is believed that especially for parts with a low volume fraction, thin walls and high surface roughness, the values of the micro porosity from CT data will be somewhat higher than that from micrographs.

For the selected four parts (10, 11, 14, 15), the internal porosity was measured with a larger amount of micrographs for 10 layers altogether and these results were compared with the results of only 4 layers. It can be seen from Table 5 that the average micro porosity per part and the corresponding standard deviation do not show a significant change. In summary, the results of the code could be verified with CT data and a small number of micrographs, e.g. 4 layers, can be used as a resource efficient way to evaluate micro porosity.

Preliminary results of the DOE modeling

As stated above, the first set of specimens was analyzed with the porosity code and Table 6 includes the resulting internal porosity. The ANOVA in Table 7 shows p-values of higher than 0.05 percent for designed pore size and its interactions. Therefore, designed pore size is categorized as a non-significant factor within the considered parameter space, when finding optimal laser power and speed to minimize internal porosity. The ANOVA in Table 8 includes only the significant factors, with laser power being the most influential, which can be seen on the highest estimate. In conclusion that means for porosity adjustment of gyroid lattices mainly laser power needs to be changed. Based on this observation, next experiments are intended to focus on process parameter development for specific wall thicknesses excluding designed cavity size as factor.

Table 3: Comparison micrographs with CT-images

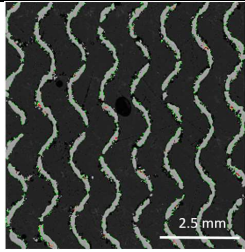
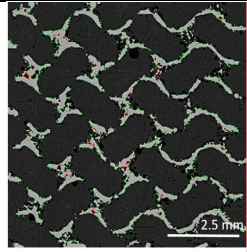
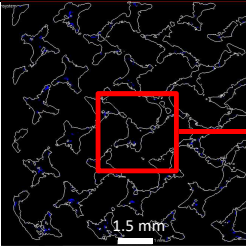
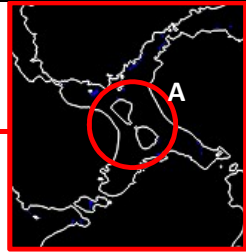
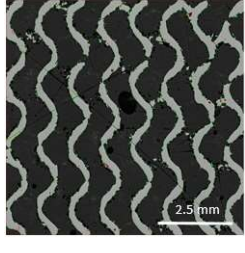
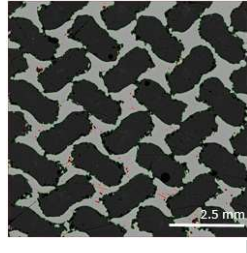
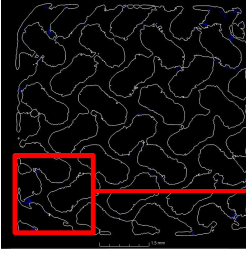
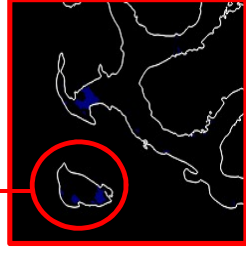
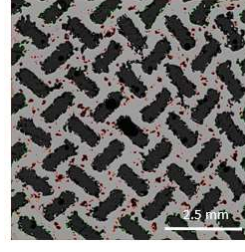
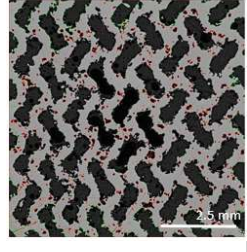
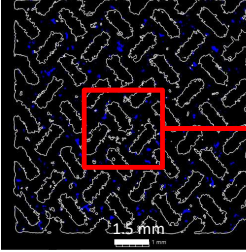
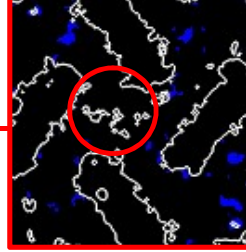
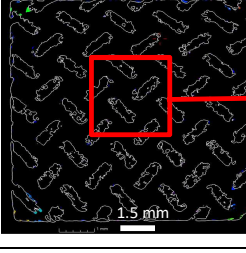
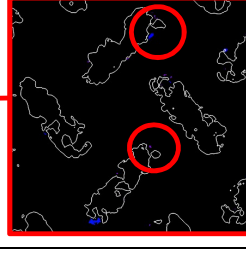
Part	Internal porosity micro-graph	Internal porosity CT-image	Etched image (complete cross-section 1)	Etched image (complete cross-section 2)	CT image (complete cross-section)	CT image (excerpt)
10	2.39%	1.59%				
11	0.53%	1.27%				
14	5.62%	3.03%				
15	0.64%	0.45%				

Table 4: CT image for ROI of part 11

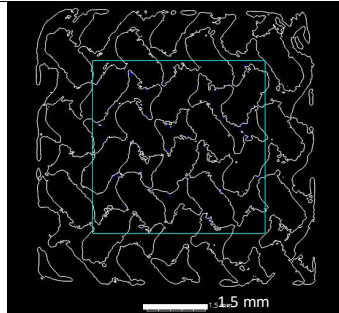
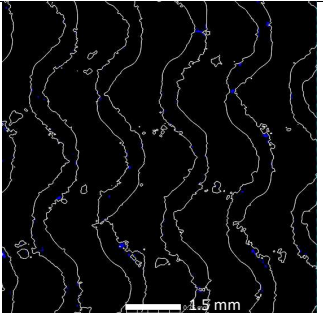
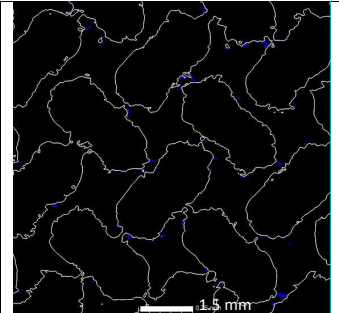
Part	Internal porosity micro-graph	Internal porosity CT-image	CT image location of the ROI	CT image ROI layer 1	CT image ROI layer 2
11	0.53%	0.81% (ROI)			

Table 5: Internal porosity and standard deviation for 4 layers versus 10 layers of micrographs

Part	Internal porosity micrograph 4 layers	Standard deviation 4 layers	Internal porosity micrograph 10 layers	Standard deviation 10 layers
10	2.39	0.89	2.04	1.03
11	0.53	0.30	0.57	0.29
14	5.62	0.52	5.53	0.62
15	0.64	0.33	0.76	0.31

Table 6: Experimental plan with resulting internal porosity

Part	Pattern of factor level	Wall thickness (µm)	Designed pore size (µm)	Laser power (W)	Scan speed (mm/s)	Internal porosity (micrograph)
1	++--	300	800	70	800	1.32
2	++++	300	800	70	1000	3.95
3	+++-	300	800	135	800	0.46
4	++++	300	800	135	1000	0.34
5	----	100	400	70	800	1.03
6	----+	100	400	70	1000	1.46
7	--+-	100	400	135	800	0.58
8	---+	100	400	135	1000	0.33
9	-+--	100	800	70	800	1.14
10	-+++	100	800	70	1000	2.39
11	-++-	100	800	135	800	0.53
12	-+++	100	800	135	1000	0.48
13	+---	300	400	70	800	2.08
14	++++	300	400	70	1000	5.62
15	+++-	300	400	135	800	0.64
16	++++	300	400	135	1000	0.68

Table 7: ANOVA p-values after first model fit

Term	Estimate	Std Error	t Ratio	Prob> t
Intercept	1.437	0.159	9.03	0.0003*
Laser power(70,135)	-0.933	0.159	-5.86	0.0020*
Laser power*Scan speed	-0.514	0.159	-3.23	0.0233*
Scan speed(800,1000)	0.469	0.159	2.95	0.0321*
Wall thickness(100,300)	0.447	0.159	2.81	0.0377*
Wall thickness*Laser power	-0.421	0.159	-2.65	0.0457*
Wall thickness*Scan speed	0.294	0.159	1.85	0.1240
Wall thickness* Designed pore size	-0.257	0.159	-1.61	0.1680
Designed pore size(400,800)	-0.113	0.159	-0.71	0.5095
Designed pore size*Laser power	0.061	0.159	0.38	0.7184
Designed pore size*Scan speed	-0.003	0.159	-0.02	0.9863

Table 8: ANOVA p-values including the significant factors only

Term	Estimate	Std Error	t Ratio	Prob> t
Intercept	1.437	0.172	8.36	<.0001*
Laser power(70,135)	-0.933	0.172	-5.43	0.0003*
Laser power*Scan speed	-0.514	0.172	-2.99	0.0136*
Scan speed(800,1000)	0.469	0.172	2.73	0.0213*
Wall thickness(100,300)	0.447	0.172	2.60	0.0265*
Wall thickness*Laser power	-0.421	0.172	-2.45	0.0342*

Conclusions

This work is originated on the goal to develop process parameters for small scale gyroid structures. One target value for optimization is internal porosity. In this work, a code to measure porosity from micrographs was presented and verified, and later applied to the first set of experimental data.

In summary, the pore analysis using CT data is mostly more exact while the micrographs only represent one layer. However, it needs to be evaluated whether the higher information accuracy is necessary justifying large resources (CT hard- and software) or if the micrographs give enough information for further work. With regard to the application of process parameter development for dental implants, it is concluded that the developed code for micrograph analysis is a resource efficient method to analyze and optimize micro-porosity. A very selective support through CT data analysis is seen as sufficient. The developed code also calculates the overall manufactured porosity (volume fraction) to analyze the accuracy. However, this data is not completely analyzed yet and will be discussed in a later work.

Regarding the process parameter development, the results classify the factor designed pore size as a non-significant parameter. Therefore, the parameter optimization with laser power as most influential factor targeting a low internal porosity for different wall thicknesses is intended as a next step.

Acknowledgements

This research is funded by the Deutsche Forschungsgemeinschaft (DFG, German Research Foundation) – Project-ID 449916462 – FOR5250. The funding support of DFG is much appreciated by authors. Additionally, authors would like to extend their gratitude to nTopology for providing access to their powerful software capabilities for design and optimization of complex geometries in this research study.

References

- [1] X. Wang, S. Xu, S. Zhou, W. Xu, M. Leary, P. Choong, M. Qian, M. Brandt, Y.M. Xie, Topological design and additive manufacturing of porous metals for bone scaffolds and orthopaedic implants: A review, *Biomaterials* 83 (2016) 127–141. <https://doi.org/10.1016/j.biomaterials.2016.01.012>.
- [2] M. Elsayed, M. Ghazy, Y. Youssef, K. Essa, Optimization of SLM process parameters for Ti6Al4V medical implants, *RPJ* 25 (2019) 433–447. <https://doi.org/10.1108/RPJ-05-2018-0112>.
- [3] A.A. Zadpoor, Mechanical performance of additively manufactured meta-biomaterials, *Acta Biomater.* 85 (2019) 41–59. <https://doi.org/10.1016/j.actbio.2018.12.038>.
- [4] A. Kumar, K.C. Nune, L.E. Murr, R.D.K. Misra, Biocompatibility and mechanical behaviour of three-dimensional scaffolds for biomedical devices: process–structure–property paradigm, *International Materials Reviews* 61 (2016) 20–45. <https://doi.org/10.1080/09506608.2015.1128310>.
- [5] H. Karcher, K. Polthier, Construction of triply periodic minimal surfaces.
- [6] H. Jinnai, Y. Nishikawa, M. Ito, S.D. Smith, D.A. Agard, R.J. Spontak, Topological Similarity of Sponge-like Bicontinuous Morphologies Differing in Length Scale, *Adv. Mater.* 14 (2002) 1615–1618. [https://doi.org/10.1002/1521-4095\(20021118\)14:22<1615:AID-ADMA1615>3.0.CO;2-S](https://doi.org/10.1002/1521-4095(20021118)14:22<1615:AID-ADMA1615>3.0.CO;2-S).
- [7] I. Maskery, L. Sturm, A.O. Aremu, A. Panesar, C.B. Williams, C.J. Tuck, R.D. Wildman, I.A. Ashcroft, R. Hague, Insights into the mechanical properties of several triply periodic minimal surface lattice structures made by polymer additive manufacturing, *Polymer* 152 (2018) 62–71. <https://doi.org/10.1016/j.polymer.2017.11.049>.
- [8] C. Yan, L. Hao, A. Hussein, P. Young, D. Raymont, Advanced lightweight 316L stainless steel cellular lattice structures fabricated via selective laser melting, *Materials & Design* 55 (2014) 533–541. <https://doi.org/10.1016/j.matdes.2013.10.027>.
- [9] A.A. Zadpoor, Bone tissue regeneration: the role of scaffold geometry, *Biomater. Sci.* 3 (2015) 231–245. <https://doi.org/10.1039/c4bm00291a>.
- [10] E. Alabort, D. Barba, R.C. Reed, Design of metallic bone by additive manufacturing, *Scripta Materialia* 164 (2019) 110–114. <https://doi.org/10.1016/j.scriptamat.2019.01.022>.
- [11] F.S.L. Bobbert, K. Lietaert, A.A. Eftekhari, B. Pouran, S.M. Ahmadi, H. Weinans, A.A. Zadpoor, Additively manufactured metallic porous biomaterials based on minimal surfaces: A unique combination of topological, mechanical, and mass transport properties, *Acta Biomater.* 53 (2017) 572–584. <https://doi.org/10.1016/j.actbio.2017.02.024>.
- [12] S. Ma, Q. Tang, X. Han, Q. Feng, J. Song, R. Setchi, Y. Liu, Y. Liu, A. Goulas, D.S. Engstrøm, Y.Y. Tse, N. Zhen, Manufacturability, Mechanical Properties, Mass-Transport Properties and Biocompatibility of Triply Periodic Minimal Surface (TPMS) Porous Scaffolds Fabricated by Selective Laser Melting, *Materials & Design* 195 (2020) 109034. <https://doi.org/10.1016/j.matdes.2020.109034>.
- [13] A. Ataee, Y. Li, M. Brandt, C. Wen, Ultrahigh-strength titanium gyroid scaffolds manufactured by selective laser melting (SLM) for bone implant applications, *Acta Materialia* 158 (2018) 354–368. <https://doi.org/10.1016/j.actamat.2018.08.005>.
- [14] S. Tsopanos, R. Mines, S. McKown, Y. Shen, W.J. Cantwell, Brooks, W., C.J. Sutcliffe, The Influence of Processing Parameters on the Mechanical Properties of Selectively Laser Melted Stainless Steel Microlattice Structures, *Journal of Manufacturing Science and Engineering* (2010).
- [15] H. Gong, K. Rafi, H. Gu, G.D. Janaki Ram, T. Starr, B. Stucker, Influence of defects on mechanical properties of Ti–6Al–4V components produced by selective laser melting and electron beam melting, *Materials & Design* 86 (2015) 545–554. <https://doi.org/10.1016/j.matdes.2015.07.147>.
- [16] R.A. Rahman Rashid, J. Mallavarapu, S. Palanisamy, S.H. Masood, A comparative study of flexural properties of additively manufactured aluminium lattice structures, *Materials Today: Proceedings* 4 (2017) 8597–8604. <https://doi.org/10.1016/j.matpr.2017.07.207>.
- [17] S. Arabnejad, R. Burnett Johnston, J.A. Pura, B. Singh, M. Tanzer, D. Pasini, High-strength porous biomaterials for bone replacement: A strategy to assess the interplay between cell morphology, mechanical properties, bone ingrowth and manufacturing constraints, *Acta Biomater.* 30 (2016) 345–356. <https://doi.org/10.1016/j.actbio.2015.10.048>.

- [18] A.M. Vilardell, A. Takezawa, A. Du Plessis, N. Takata, P. Krakhmalev, M. Kobashi, I. Yadroitsava, I. Yadroitsev, Topology optimization and characterization of Ti6Al4V ELI cellular lattice structures by laser powder bed fusion for biomedical applications, *Materials Science and Engineering: A* 766 (2019) 138330. <https://doi.org/10.1016/j.msea.2019.138330>.
- [19] D. Mahmoud, M.A. Elbestawi, Selective laser melting of porosity graded lattice structures for bone implants, *Int J Adv Manuf Technol* 100 (2019) 2915–2927. <https://doi.org/10.1007/s00170-018-2886-9>.
- [20] R. Hedayati, H. Hosseini-Toudeshky, M. Sadighi, M. Mohammadi-Aghdam, A.A. Zadpoor, Computational prediction of the fatigue behavior of additively manufactured porous metallic biomaterials, *International Journal of Fatigue* 84 (2016) 67–79. <https://doi.org/10.1016/j.ijfatigue.2015.11.017>.
- [21] A. Du Plessis, S. Razavi, F. Berto, The effects of microporosity in struts of gyroid lattice structures produced by laser powder bed fusion, *Materials & Design* 194 (2020) 108899. <https://doi.org/10.1016/j.matdes.2020.108899>.
- [22] C.N. Kelly, J. Francovich, S. Julmi, D. Safranski, R.E. Guldborg, H.J. Maier, K. Gall, Fatigue behavior of As-built selective laser melted titanium scaffolds with sheet-based gyroid microarchitecture for bone tissue engineering, *Acta Biomater.* 94 (2019) 610–626. <https://doi.org/10.1016/j.actbio.2019.05.046>.
- [23] E. Sallica-Leva, A.L. Jardini, J.B. Fogagnolo, Microstructure and mechanical behavior of porous Ti-6Al-4V parts obtained by selective laser melting, *J. Mech. Behav. Biomed. Mater.* 26 (2013) 98–108. <https://doi.org/10.1016/j.jmbbm.2013.05.011>.
- [24] D. Mahmoud, M. Elbestawi, Lattice Structures and Functionally Graded Materials Applications in Additive Manufacturing of Orthopedic Implants: A Review, *JMMP* 1 (2017) 13. <https://doi.org/10.3390/jmmp1020013>.
- [25] P. Hanzl, M. Zetek, T. Bakša, T. Kroupa, The Influence of Processing Parameters on the Mechanical Properties of SLM Parts, *Procedia Engineering* 100 (2015) 1405–1413. <https://doi.org/10.1016/j.proeng.2015.01.510>.
- [26] A. Du Plessis, I. Yadroitsava, I. Yadroitsev, S.G. Le Roux, D.C. Blaine, Numerical comparison of lattice unit cell designs for medical implants by additive manufacturing, *Virtual and Physical Prototyping* 13 (2018) 266–281. <https://doi.org/10.1080/17452759.2018.1491713>.
- [27] F.P.W. Melchels, K. Bertoldi, R. Gabbriellini, A.H. Velders, J. Feijen, D.W. Grijpma, Mathematically defined tissue engineering scaffold architectures prepared by stereolithography, *Biomaterials* 31 (2010) 6909–6916. <https://doi.org/10.1016/j.biomaterials.2010.05.068>.
- [28] T.G. Spears, S.A. Gold, In-process sensing in selective laser melting (SLM) additive manufacturing, *Integr Mater Manuf Innov* 5 (2016) 16–40. <https://doi.org/10.1186/s40192-016-0045-4>.
- [29] D. Wiczorek, Statistische Versuchsplanung, in: G. Bandow, H.H. Holzmüller (Eds.), "Das ist gar kein Modell!": Unterschiedliche Modelle und Modellierungen in Betriebswirtschaftslehre und Ingenieurwissenschaften, first. Auflage, Gabler Research, Wiesbaden, 2010, pp. 167–187.
- [30] W. Kleppmann, Taschenbuch Versuchsplanung: Produkte und Prozesse optimieren, seventh., aktual. und erw. Aufl., Hanser, München, 2011.
- [31] H. Shipley, D. McDonnell, M. Culleton, R. Coull, R. Lupoi, G. O'Donnell, D. Trimble, Optimisation of process parameters to address fundamental challenges during selective laser melting of Ti-6Al-4V: A review, *International Journal of Machine Tools and Manufacture* 128 (2018) 1–20. <https://doi.org/10.1016/j.ijmachtools.2018.01.003>.
- [32] U. Scipioni Bertoli, A.J. Wolfer, M.J. Matthews, J.-P.R. Delplanque, J.M. Schoenung, On the limitations of Volumetric Energy Density as a design parameter for Selective Laser Melting, *Materials & Design* 113 (2017) 331–340. <https://doi.org/10.1016/j.matdes.2016.10.037>.
- [33] N. Emminghaus, R. Bernhard, J. Hermsdorf, S. Kaielerle, Determination of optimum process parameters for different Ti-6Al-4V powders processed by Laser-based Powder Bed Fusion, *Procedia CIRP* 111 (2022) 134–137. <https://doi.org/10.1016/j.procir.2022.08.052>.

Note

A version of the code can be provided electronically. Please email A.Jahn@LZH.de